Available online at www.sciencedirect.com
ScienceDirect
Comput. Methods Appl. Mech. Engrg. 196 (2006) 437–451
Computer methods in applied mechanics and engineering
www.elsevier.com/locate/cma

hp Discontinuous Galerkin methods for advection dominated problems in shallow water flow

Ethan J. Kubatko [a], Joannes J. Westerink [a], Clint Dawson [b,*]

[a] *Department of Civil Engineering and Geological Sciences, University of Notre Dame, Notre Dame, IN 46556, United States*
[b] *Institute for Computational Engineering and Sciences, The University of Texas at Austin, Austin, TX 7871, United States*

Received 22 September 2005; received in revised form 21 April 2006; accepted 3 May 2006

Abstract

In this paper, we discuss the development, verification, and application of an *hp* discontinuous Galerkin (DG) finite element model for solving the shallow water equations (SWE) on unstructured triangular grids. The *h* and *p* convergence properties of the method are demonstrated for both linear and highly nonlinear problems with advection dominance. Standard *h*-refinement for a fixed *p* leads to $p+1$ convergence rates, while exponential convergence is observed for *p*-refinement for a fixed *h*. It is also demonstrated that the use of *p*-refinement is more efficient for problems exhibiting smooth solutions. Additionally, the ability of *p*-refinement to adequately resolve complex, two-dimensional flow structures is demonstrated in the context of a coastal inlet problem.

Keywords: Discontinuous Galerkin method; Shallow water equations; Advection

1. Introduction

The shallow water equations (SWE) are extensively applied to model flows in coastal oceans, inlets, rivers and adjacent floodplains. These equations include two numerically troublesome processes that have led to intensive algorithmic development over the past four decades. The SWE are, in their simplest form, long wave propagation equations and numerical solutions are often plagued by energetic artificial spurious modes that appear even in solutions of the fully linear SWE and are independent of the level of wave form resolution [1–3]. In addition, the nonlinear advective acceleration terms can lead to the generation of spurious modes associated with phase errors for poorly resolved scales. The numerical difficulties associated with the wave propagation and advection processes have traditionally been solved using distinct algorithms. For continuous Galerkin (CG) finite element solutions, successful techniques to the spurious mode problem associated with wave propagation include reformulating the governing equations [4,5] or using grid enriched velocity solutions [6]. The nonlinear advective terms have been approached with algorithms such as the streamline upwind Petrov–Galerkin (SUPG) method [7] or fractional step methods which implement Lagrangian tracking to solve for the advection process [8]. Although these techniques have made progress towards solving the fully nonlinear form of the SWE, robustness, accuracy and artificial damping problems remain.

Recently discontinuous Galerkin (DG) methods applied to the SWE have emerged and provide a unified approach to solving the numerical difficulties associated with both the wave propagation and advection processes. The main advantages of DG methods for shallow water flows are: their ability to capture smooth physically damped solutions to the wave propagation problem; their ability to handle advection dominated flows including problems with hydraulic jumps or bores (discontinuities); their inherent elemental mass and momentum conservation properties, which make them ideal for coupling flow and transport

* Corresponding author. Tel.: +1 512 4713312; fax: +1 512 4718694.
E-mail addresses: ekubatko@nd.edu (E.J. Kubatko), jjw@photius.ce.nd.edu (J.J. Westerink), clint@ices.utexas.edu (C. Dawson).

0045-7825/$ - see front matter © 2006 Elsevier B.V. All rights reserved.
doi:10.1016/j.cma.2006.05.002

models; and the ease with which both h (grid) and p (polynomial order) refinement, and also adaptivity can be implemented. In this paper, we discuss the development, verification, and application of an hp DG finite element model for solving the SWE on unstructured triangular grids. In particular, we focus on applications involving advection dominated SWE using high-order p solutions.

Although DG methods first appeared in the 1970s (see for example [9]), application of these methods to the SWE has only appeared in the literature in the past 5 years, and most of these studies have focused primarily on the application of the method to specialized problems involving dam break flows and hydraulic jumps and/or have employed essentially low-order p approximations [10–14]. It is only very recently that hp (or spectral) DG methods employing high-order p approximations have been preliminarily investigated for the SWE [15–17]. In [15,17] high-order *global* DG SWE models, which solve the equations on the sphere using curvilinear quadrilateral elements, were developed and applied to a number of tests cases for problems of a global scale (e.g. global, steady-state, geostrophic flow). Both approaches used the local Lax–Friedrich (LLF) flux as the Riemann solver. In [16], a high-order DG SWE model using triangular elements was developed that solves the so-called divergence form of the equations and makes use of the HLLC Riemann solver. The hp convergence properties of the model were demonstrated for a simple linear problem.

The present study differs from these previous studies in terms of the details of the implementation, the problems examined, and the assessment of the method in terms of hp convergence properties. With regard to the details of the implementation, the DG method presented solves the so-called Green's form of the equations making use of approximating polynomials of arbitrary order over triangular elements that are linked through a numerical flux approximated using Roe's method. In order to maintain computational efficiency for high-order implementations of the method, an orthogonal and hierarchical triangular basis is used along with efficient symmetrical Gaussian quadrature rules that are optimal (or near optimal) for the triangle. This results in a matrix-free algorithm that uses a minimum number of quadrature points.

In terms of the problems that are examined and the assessment of the method, previous convergence studies have typically been limited to simplified steady-state or linear problems without the presence of source/sink terms, spatially varying bathymetry, or time-varying boundary conditions – factors that are essential to include for an assessment of the method's potential to model realistic flow scenarios in coastal engineering problems. In this paper, we examine a linear channel problem, a fully nonlinear channel problem with spatially varying bathymetry, and a fully nonlinear inlet problem with an ebb shoal. The latter problems are strongly advection dominated, with the inlet problem involving the formation, development and advection of energetic eddies. The hp convergence properties of the DG method are rigorously assessed for these linear and nonlinear problems. Through systematic h and p refinement, the dual paths to convergence of the method are demonstrated. Although no theoretical convergence rates are known for DG methods that incorporate complex numerical fluxes (such as the HLLC or Roe flux) applied to the fully nonlinear SWE without eddy viscosity, previous numerical results using hp DG methods have shown h-convergence rates of $p+1$ and exponential p-convergence rates for linear problems (see for example [16,18]; also see [19] for a theoretical result that considers a viscous form of the SWE and uses upwind fluxes). In this paper, for both linear and nonlinear problems, we demonstrate that standard h refinement for a fixed p leads to convergence rates of approximately $p+1$, while exponential convergence is observed for p refinement on a fixed mesh. It is also demonstrated that the use of p refinement is more efficient for problems exhibiting smooth solutions. Additionally, the ability of p-refinement to adequately resolve complex two-dimensional flow structures is investigated in the context of a coastal inlet problem.

This paper is organized as follows. In the next section, the SWE equations are presented. We then proceed with a detailed description of our implementation of the DG method for the two-dimensional SWE's, including specific details on the numerical flux, basis, and quadrature rules that are employed. In Section 4, numerical results are presented and the performance of the method is evaluated in a series of test cases ranging in complexity from smooth linear problems to highly nonlinear, advection dominated flow scenarios. Section 5 summarizes this work and discusses future developments in this area using DG methods.

2. Governing equations

The two-dimensional SWE consist of the depth-averaged continuity equation and the x and y momentum equations written here in conservative form

$$\frac{\partial \zeta}{\partial t} + \frac{\partial}{\partial x}(Hu) + \frac{\partial}{\partial y}(Hv) = 0, \tag{1}$$

$$\frac{\partial}{\partial t}(uH) + \frac{\partial}{\partial x}\left(Hu^2 + \frac{1}{2}g(H^2 - h^2)\right) + \frac{\partial}{\partial y}(Huv) = g\zeta\frac{\partial h}{\partial x} - \tau uH + F_x, \tag{2}$$

$$\frac{\partial}{\partial t}(vH) + \frac{\partial}{\partial x}(Huv) + \frac{\partial}{\partial y}\left(Hv^2 + \frac{1}{2}g(H^2 - h^2)\right) = g\zeta\frac{\partial h}{\partial y} - \tau vH + F_y, \tag{3}$$

where ζ is the elevation of the free surface measured from the geoid (positive upwards), h is the bathymetric depth measured from the geoid (positive downwards), $H = \zeta + h$ is the total height of the water column, g is the gravitational constant, u and v are the depth-averaged velocities in the x and y directions respectively, τ is the bottom friction factor, and F_x and F_y are meant to represent any additional terms which may be present due to Coriolis

force, tidal potential forces, surface stresses such as wind or wave radiation stresses, etc. The specific functional form of these additional terms is not important in the details of the algorithm to be outlined. Eqs. (1)–(3) are supplemented with suitable initial and boundary conditions.

Note that the equations have been written in so-called divergence form. That is, each equation takes the form

$$\frac{\partial w_i}{\partial t} + \nabla \cdot \mathbf{F}_i(\mathbf{w}) = s_i(\mathbf{w}), \tag{4}$$

where $i = 1$, 2, or 3 and w_i is the ith component of the vector $\mathbf{w}$ of conserved variables

$$\mathbf{w} = [\,\zeta, \quad uH, \quad vH\,]^{\mathrm{T}}, \tag{5}$$

$\mathbf{F}_i$ is the ith row of the flux function matrix whose columns are the flux function vectors in the x and y directions denoted by $\mathbf{f}_x$ and $\mathbf{f}_y$ respectively:

$$\mathbf{F} = [\,\mathbf{f}_x, \quad \mathbf{f}_y\,] = \begin{bmatrix} uH & vH \\ Hu^2 + \frac{1}{2}g(H^2 - h^2) & Huv \\ Huv & Hv^2 + \frac{1}{2}g(H^2 - h^2) \end{bmatrix} \tag{6}$$

and finally s_i is the ith component of the vector $\mathbf{s}$ of source/sink terms which is given by

$$\mathbf{s} = \left[0, \quad g\zeta\frac{\partial h}{\partial x} + F_x - \tau uH, \quad g\zeta\frac{\partial h}{\partial y} + F_y - \tau vH\right]^{\mathrm{T}}. \tag{7}$$

With these definitions, the equations can be written in the concise form

$$\frac{\partial \mathbf{w}}{\partial t} + \frac{\partial \mathbf{f}_x}{\partial x} + \frac{\partial \mathbf{f}_y}{\partial y} = \mathbf{s}. \tag{8}$$

3. Discontinuous Galerkin method

We first introduce notation that will be used. Given a domain $\Omega \subset \mathbb{R}^2$, which has been triangulated into a set of non-overlapping, but not necessarily conforming, elements, let Ω_e define the domain of an element e and denote the boundary of the element by $\partial\Omega_e$. An inner product taken over Ω_e will be denoted by $(\cdot,\cdot)_{\Omega_e}$, and an inner product taken over $\partial\Omega_e$ will be denoted by $\langle\cdot,\cdot\rangle_{\partial\Omega_e}$. The outward unit normal vector of $\partial\Omega_e$ will be denoted by $\mathbf{n}$, and the fixed unit normal vector for a given edge i of $\partial\Omega_e$ will be denoted by $\mathbf{n}_i$.

We approximate $\mathbf{w}$ by $\mathbf{w}_h$, the components of which belong to the space of piecewise smooth functions that are differentiable over an element, but which allow discontinuities between elements. We denote this space of functions by V_h. The value of a function $v \in V_h$ along $\partial\Omega_e$ is denoted by $v^{(\mathrm{in})}$ when approaching $\partial\Omega_e$ from the interior of an element e and by $v^{(\mathrm{ex})}$ when approaching $\partial\Omega_e$ from the exterior of an element.

The SWE are put into a discrete weak form by replacing $\mathbf{w}$ by $\mathbf{w}_h$, multiplying each equation by a test function $v \in V_h$, integrating over each element, and integrating the divergence term by parts

$$\left(\frac{\partial}{\partial t}(w_h)_i, v\right)_{\Omega_e} - (\nabla v, \mathbf{F}_i)_{\Omega_e} + \langle \mathbf{F}_i \cdot \mathbf{n}, v\rangle_{\partial\Omega_e} = (s, v)_{\Omega_E} \quad i = 1,2,3, \tag{9}$$

where $(w_h)_i$ is the ith component of $\mathbf{w}_h$. Due to the fact that discontinuities are permitted along $\partial\Omega_e$, the flux $\mathbf{F}$, which may be dual-valued along $\partial\Omega_e$, is replaced in the boundary integral by a single-valued numerical flux denoted by $\widehat{\mathbf{F}}$. Making this substitution the discrete weak formulation of the problem is now given by

$$\left(\frac{\partial}{\partial t}(w_h)_i, v\right)_{\Omega_e} - (\nabla v, \mathbf{F}_i)_{\Omega_e} + \langle \widehat{\mathbf{F}}_i \cdot \mathbf{n}, v\rangle_{\partial\Omega_e} = (s, v)_{\Omega_E}, \quad i = 1,2,3, \tag{10}$$

where $\widehat{\mathbf{F}}_i$ is the ith row of $\widehat{\mathbf{F}}$.

To complete the spatial discretization, we must now define the procedure used to calculate the numerical flux, the choice of basis functions, and the method used to evaluate the integrals of Eq. (10). This is done in the following sub-sections.

3.1. The numerical flux – solving the Riemann problem

To define the numerical flux, it is useful to begin by computing the Jacobian matrices of the x and y flux function vectors

$$\mathbf{J}_x = \frac{\partial \mathbf{f}_x}{\partial \mathbf{w}} = \begin{bmatrix} 0 & 1 & 0 \\ gH - u^2 & 2u & 0 \\ -uv & v & u \end{bmatrix}, \quad \mathbf{J}_y = \frac{\partial \mathbf{f}_y}{\partial \mathbf{w}} = \begin{bmatrix} 0 & 0 & 1 \\ -uv & v & u \\ gH - v^2 & 0 & 2v \end{bmatrix} \tag{11}$$

and a "normal Jacobian matrix" defined by

$$\mathbf{J}_n = \mathbf{J}_x n_x + \mathbf{J}_y n_y, \tag{12}$$

where n_x and n_y are the x and y components, respectively, of the unit normal vector, $\mathbf{n}$. This matrix has the following eigenvalues:

$$\lambda_1 = un_x + vn_y - \sqrt{gH}, \quad \lambda_2 = un_x + vn_y, \quad \lambda_3 = un_x + vn_y + \sqrt{gH} \tag{13}$$

and the corresponding eigenvectors

$$\mathbf{r}_1 = \begin{bmatrix} 1 \\ u - \sqrt{gH}n_x \\ v - \sqrt{gH}n_y \end{bmatrix}, \quad \mathbf{r}_2 = \begin{bmatrix} 0 \\ -n_y \\ n_x \end{bmatrix}, \quad \mathbf{r}_3 = \begin{bmatrix} 1 \\ u + \sqrt{gH}n_x \\ v + \sqrt{gH}n_y \end{bmatrix}. \tag{14}$$

Using these eigenvalues and eigenvectors we define the following matrices:

$$|\boldsymbol{\lambda}| = \begin{bmatrix} |\lambda_1| & 0 & 0 \\ 0 & |\lambda_2| & 0 \\ 0 & 0 & |\lambda_3| \end{bmatrix}, \quad \mathbf{R} = [\mathbf{r}_1, \quad \mathbf{r}_2, \quad \mathbf{r}_3]. \tag{15}$$

A thorough discussion of the Riemann problem and its solution, both in a theoretical and numerical framework, is presented by [20]. There are a number of different approaches that can be used. In our formulation, we use Roe's method [21] to solve the Riemann problem, which is known to provide sharp resolution of the solution at discontinuities [22]. We have tested Roe's flux for a variety of problems, and it has proven to be robust. Other flux approximations will be tested in future work.

Using the definitions above, Roe's numerical flux can be written in the form

$$\widehat{\mathbf{F}} = \frac{1}{2}\left[\mathbf{F}_n\left(\mathbf{w}_h^{(\mathrm{in})}\right) + \mathbf{F}_n\left(\mathbf{w}_h^{(\mathrm{ex})}\right)\right] - \frac{1}{2}\widehat{\mathbf{R}}|\hat{\lambda}|\widehat{\mathbf{R}}^{-1}\left(\mathbf{w}_h^{(\mathrm{in})} - \mathbf{w}_h^{(\mathrm{ex})}\right), \tag{16}$$

where $\mathbf{F}_n$ is a vector whose ith component is defined by

$$(\mathbf{F}_n)_i = \mathbf{F}_i \cdot \mathbf{n}, \tag{17}$$

and where $\widehat{\mathbf{R}}$ and $|\hat{\lambda}|$ are made up of the eigenvectors and eigenvalues, respectively, of the linearized normal Jacobian matrix which is Eq. (12) evaluated at the so-called "Roe averages":

$$\begin{aligned} \hat{\zeta} &= \frac{1}{2}\left(\zeta^{(\mathrm{in})} + \zeta^{(\mathrm{ex})}\right), \\ \hat{u} &= \frac{u^{(\mathrm{in})}\sqrt{H^{(\mathrm{in})}} + u^{(\mathrm{ex})}\sqrt{H^{(\mathrm{ex})}}}{\sqrt{H^{(\mathrm{in})}} + \sqrt{H^{(\mathrm{ex})}}}, \\ \hat{v} &= \frac{v^{(\mathrm{in})}\sqrt{H^{(\mathrm{in})}} + v^{(\mathrm{ex})}\sqrt{H^{(\mathrm{ex})}}}{\sqrt{H^{(\mathrm{in})}} + \sqrt{H^{(\mathrm{ex})}}}. \end{aligned} \tag{18}$$

3.2. The basis

A judicious choice of basis can simplify the implementation of the method and improve the computational efficiency. Here, we employ an orthogonal triangular basis due to Dubiner [23], which has been extensively used in the DG literature. This basis results in a diagonal mass matrix, which is trivially inverted. The basis is also hierarchical implying that higher-order elements are obtained by simply adding terms to the lower-order elements, i.e. a quadratic element is obtained by adding additional "modes" to the linear element. This property is especially advantageous in implementing p-adaptivity. Unlike standard Lagrangian bases, which are typically used in continuous Galerkin finite element methods, the degrees of freedom in this basis correspond to different "modal" coefficients of the solution rather than specific nodal values.

The basis is constructed as a (generalized) tensor product of polynomials

$$\phi_{ij}(\xi_1, \xi_2) = P_i^{0,0}(\eta_1)\left(\frac{1-\eta_2}{2}\right)^i P_j^{2i+1,0}(\eta_2), \tag{19}$$

where $P_N^{\alpha,\beta}$ is the Nth order Jacobi polynomial of weights α and β, ξ_i are the coordinates of the master triangular element, and η_i are the coordinates given by the transformation:

$$\eta_1 = \frac{2(1+\xi_1)}{(1-\xi_2)} - 1, \quad \eta_2 = \xi_2. \tag{20}$$

This transformation effectively maps the triangular master element into a quadrilateral one as shown in Fig. 1. It is noted that there is a singularity in the transformation given by Eq. (20) at $\xi_2 = 1$. However, as noted in [18], even though the transformation is singular, the basis functions, ϕ_{ij} are not singular functions in terms of the ξ-coordinates. They are in fact polynomials. The $\frac{1-\eta_2}{2}$ term appearing in ϕ_{ij} ensures this. For example, the basis function for $i = 1, j = 0$ expressed in the ξ-coordinates is

$$\begin{aligned} \phi_{10} &= \left[\frac{2(1+\xi_1)}{1-\xi_2} - 1\right]\left(\frac{1-\xi_2}{2}\right)(1) \\ &= \frac{2(1+\xi_1)}{\cancel{1-\xi_2}}\left(\frac{\cancel{1-\xi_2}}{2}\right) - \left(\frac{1-\xi_2}{2}\right) \\ &= \xi_1 + \frac{1}{2}\xi_2 + \frac{1}{2}. \end{aligned} \tag{21}$$

Thus, the basis functions ϕ_{ij} are polynomials both in terms of ξ- and η-coordinate systems.

With this basis the approximate solution is now defined as

$$\mathbf{w}_h = \sum_i \sum_j \tilde{\mathbf{w}}_{ij}\phi_{ij}, \tag{22}$$

where $\tilde{\mathbf{w}}_{ij}$ are the modal degrees of freedom. Due to the hierarchical nature of basis, a linear element is obtained by using the first three functions, a quadratic element by using the first six, and so on.

3.3. Quadrature rules

The integrals appearing in Eq. (10) are typically evaluated using quadrature rules, although a quadrature free DG method has been implemented as well [24]. Note that both an area integral and a boundary integral, which

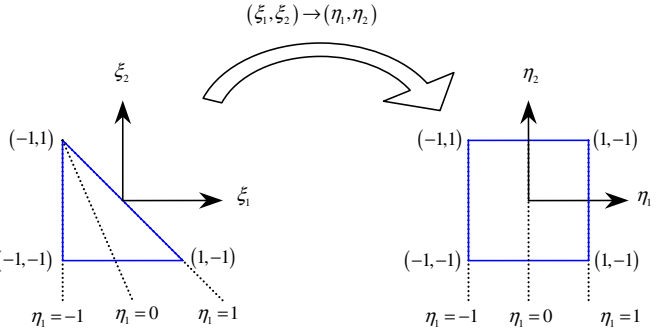

Fig. 1. Transformation of the master triangular element into a quadrilateral element.

resulted from the integration by parts, need to be evaluated. For a DG spatial approximation of degree p, the area and boundary integrals should be integrated with $2p$ and $2p+1$ Gaussian quadrature rules, respectively [25]. The boundary integrals can be evaluated using standard one-dimensional Gaussian quadrature rules. Typically for *hp* or spectral versions of the DG method using triangular elements, the area integrals are evaluated using a product of one-dimensional Gaussian quadrature rules over the master quadrilateral element (see for example [16,26]). In our implementation, instead of using this procedure, we have employed efficient high-degree symmetric Gaussian quadrature rules specifically for the triangle as defined in [27], which gives quadrature rules for the triangle up to degree 20. Use of these quadrature rules results in a lower number of Gauss points when compared to using a product of one-dimensional Gaussian quadrature rules over a quadrilateral. For example, for a $p=4$ spatial approximation 25 quadrature points are required for the area integral when using a product rule while only 16 points are required when using the quadrature rule for the triangle.

3.4. The Runge–Kutta time discretization

The DG spatial discretization reduces the problem to a system of ODE's. After inverting the mass matrix (which is diagonal and therefore trivially inverted), we can write the systems of ODE's in the following concise form:

$$\frac{\mathrm{d}}{\mathrm{d}t}(\mathbf{w}_h) = L_h(\mathbf{w}_h). \tag{23}$$

We discretize this system of ODE's using explicit total variation diminishing (TVD) Runge–Kutta schemes, which were first introduced by Shu and Osher, [28,29]. We note that these schemes preserve the TVD property of the DG spatial discretization and the forward Euler method with the application of a slope limiter [30]. For a linear or $p=1$ spatial approximation we use a second-order scheme which is given by

$$\begin{aligned}\mathbf{w}_h^{(1)} &= \mathbf{w}_h^{(t)} + \Delta t L_h\left(\mathbf{w}_h^{(t)}\right),\\ \mathbf{w}_h^{(t+1)} &= \frac{1}{2}\left(\mathbf{w}_h^{(t)} + \mathbf{w}_h^{(1)} + \Delta t L_h\left(\mathbf{w}_h^{(1)}\right)\right).\end{aligned} \tag{24}$$

For spatial approximations of order $p>1$ we use a third-order scheme

$$\begin{aligned}\mathbf{w}_h^{(1)} &= \mathbf{w}_h^{(t)} + \Delta t L_h\left(\mathbf{w}_h^{(t)}\right),\\ \mathbf{w}_h^{(2)} &= \frac{3}{4}\mathbf{w}_h^{(t)} + \frac{1}{4}\left(\mathbf{w}_h^{(1)} + \Delta t L_h\left(\mathbf{w}_h^{(1)}\right)\right),\\ \mathbf{w}_h^{(t+1)} &= \frac{3}{4}\mathbf{w}_h^{(t)} + \frac{2}{3}\left(\mathbf{w}_h^{(2)} + \Delta t L_h\left(\mathbf{w}_h^{(2)}\right)\right).\end{aligned} \tag{25}$$

Due to the fact that these schemes are explicit, the size of the timestep is limited by a CFL condition. In practice, we take

$$\Delta t \leqslant \min_{\Omega_e}\left(\frac{h_e}{(\lambda_{\max})_e(2p+1)}\right), \tag{26}$$

where h_e is the diameter of the element and $\lambda_{\max}$ is an estimate of the maximum (in absolute value) of the eigenvalues given by Eq. (13) for an element e. The factor of $1/(2p+1)$ is an estimate of the CFL number required for stability (see [30]).

3.5. The slope limiter

When the solution displays sharp fronts or shocks the application of a slope limiter at each intermediate time step of the schemes described above can be used in order to control local oscillations. This procedure may reduce the order

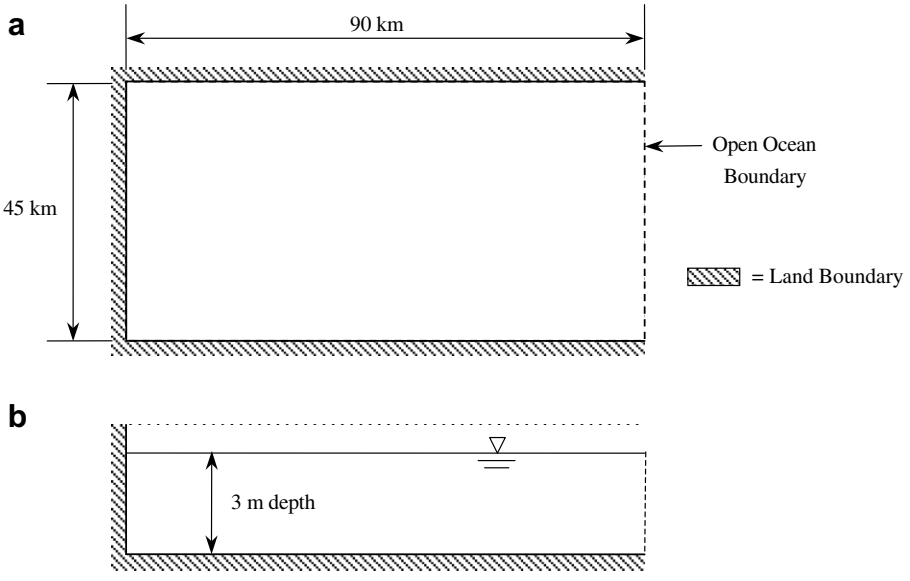

Fig. 2. Domain of problems P1.1 and P1.2: (a) plan view problems P1.1 and P1.2; (b) cross section problem P1.1.

of the approximation in the neighborhood of the sharp front if an oscillation is detected. For the problems considered in this paper, we have found it unnecessary in practice to apply any kind of limiting.

3.6. Boundary conditions

Boundary conditions are enforced weakly through the numerical flux by specifying appropriate exterior values for the variables along boundary edges.

No-normal flow or land boundaries are enforced by specifying the following exterior conditions:

$$Q_n^{(\mathrm{ex})} = -Q_{\mathrm{n}}^{(\mathrm{in})}, \quad Q_{\mathrm{t}}^{(\mathrm{ex})} = Q_{\mathrm{t}}^{(\mathrm{in})}, \quad \zeta^{(\mathrm{ex})} = \zeta^{(\mathrm{in})}, \tag{27}$$

where Q_{n} are Q_{t} are the flow rates in the normal and tangential directions of the given edge, respectively.

At open water boundaries prescribed surface elevations, $\zeta^{\mathrm{b.c.}}$, or flow rates, $\mathbf{Q}^{\mathrm{b.c.}}$ are specified as exterior values of the corresponding variable. The remaining variables are simply set equal to their corresponding interior values. That is, for an elevation specified open boundary condition we specify:

$$\zeta^{(\mathrm{ex})} = \zeta^{\mathrm{b.c.}}, \quad \mathbf{Q}^{(\mathrm{ex})} = \mathbf{Q}^{(\mathrm{in})}. \tag{28}$$

and for a flow specified open boundary condition we specify:

$$\mathbf{Q}^{(\mathrm{ex})} = \mathbf{Q}^{\mathrm{b.c.}}, \quad \zeta^{(\mathrm{ex})} = \zeta^{(\mathrm{in})}. \tag{29}$$

In some cases for higher-order approximations ($p \geqslant 3$), the elevation specified boundary condition has led to instabilities occurring at or near corners or when the flow is nearly parallel to the boundary as is the case when interior generated eddies propagate to the open boundary. It was found that this problem can be avoided by specifying a zero exterior tangential flow along the given edge or by specifying an equivalent flow specified boundary condition. The proper specification of open ocean boundary conditions in the framework of the DG method is currently being investigated.

In the case of a radiation boundary condition, we simply set the exterior values of all the variables to their corresponding interior values.

4. Numerical examples

The DG method outlined above has been applied to a number of problems varying from linear to highly nonlinear. In this section, the results of three sets of test cases, which are described in the following sub-sections, are presented. In cases where the error is evaluated, it is computed at the barycenter of each element in the domain by comparing the numerical solution to either an analytical or highly refined numerical solution. We then define the maximum or L^∞ error as the maximum (in absolute value) of the errors over all of the elements.

4.1. Problems P1.1 and P1.2: Rectangular harbor with linear SWE

In the first problem, we look at a linear wave propagation problem by solving the linear SWE, which are obtained from Eqs. (1)–(3) by neglecting the advective terms, assuming the height of the free surface is small compared to the total depth, and using a linear bottom friction. Thus the linear SWE equations take the form

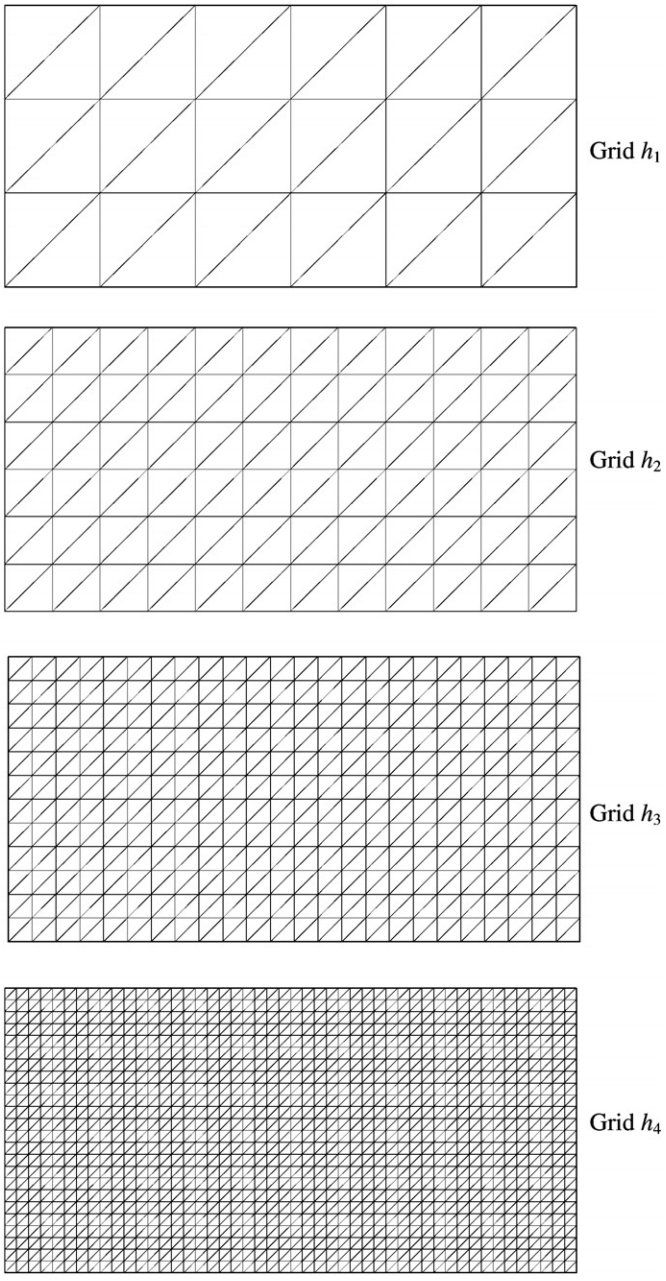

Fig. 3. h Refinements for problems P1.1 and P1.2.

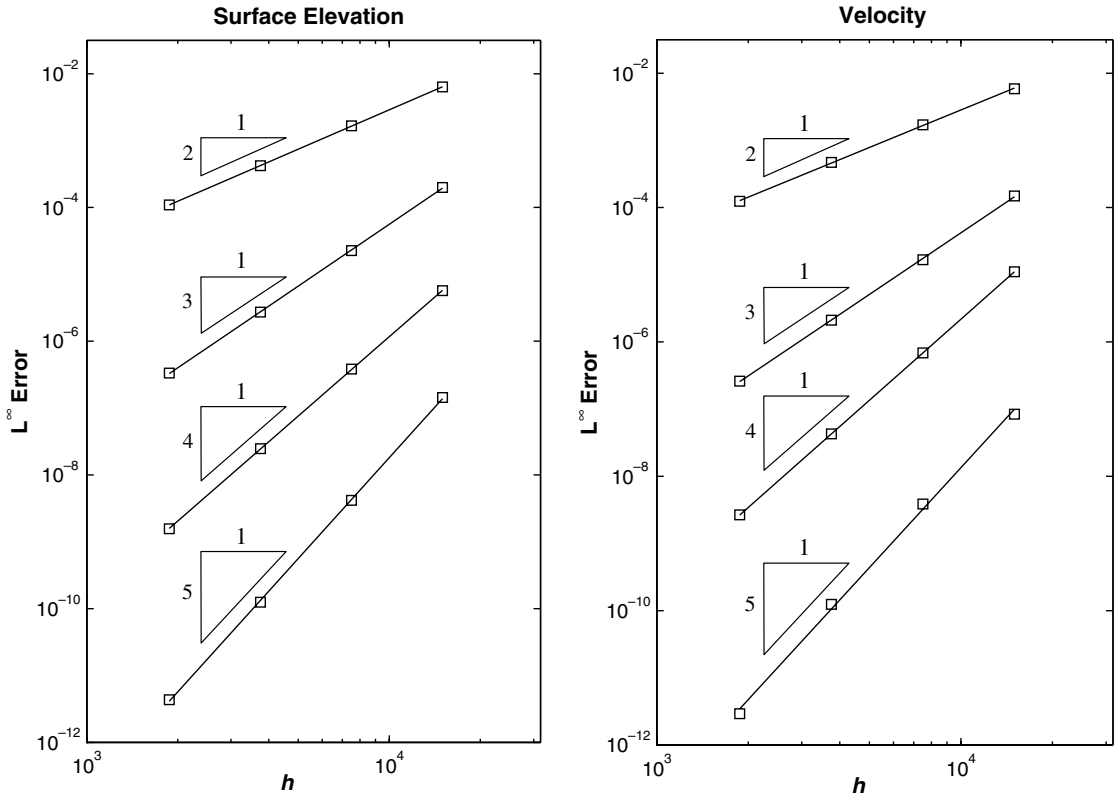

Fig. 4. h Convergence for problem P1.1 in surface elevation and velocity.

$$\frac{\partial \zeta}{\partial t} + \frac{\partial}{\partial x}(hu) + \frac{\partial}{\partial y}(hv) = 0, \tag{30}$$

$$\frac{\partial u}{\partial t} + g\frac{\partial \zeta}{\partial x} = -\tau u, \tag{31}$$

$$\frac{\partial v}{\partial t} + g\frac{\partial \zeta}{\partial y} = -\tau v. \tag{32}$$

For these equations Lynch and Gray [31] derive analytical solutions to a number of geometrically idealized estuary problems that are meant to serve as verification tools for shallow water models. In an effort to make these problems rigorous test cases, they incorporate tidal forcing, bottom friction, wind stress, spatially varying bathymetries, and both Cartesian and polar geometries. By linearizing the shallow water equations and restricting themselves to periodic forcing functions, they obtain a number of dynamic steady-state solutions.

Here, we present solutions to the flat bathymetry Cartesian geometry case (see Table 2 of [31]) both with and without linear bottom friction, i.e. $\tau = \text{constant}$. Although not presented here, the method has also been applied to the cases of linear and quadratic varying bathymetry as well. The domains of the problem are defined as rectangular harbors with land boundaries on the north, south, and west (specified by no normal flow) and an open ocean boundary on the east (specified by an elevation). The harbors, shown in Fig. 2, are defined as 45,000 m wide in the north–south direction and 90,000 m long in the east–west direction. The problems are forced with a 0.30 m amplitude M_2 tidal signal. We examine the flat bathymetry case both without bottom friction (denoted P1.1) and with linear bottom friction, $\tau = 0.0001\ \text{s}^{-1}$ (denoted P1.2). In both cases, the linear SWE equations are solved, and the initial conditions are defined according to the exact solution at time $t = 0$. A time step of 1 s is used for all the simulations, which is well below the estimate provided by Eq. (26). This was done to insure that the spatial errors were the dominant part of the overall error since we are primarily interested in the rate of convergence of the DG spatial discretization.

Table 1
Computed orders of convergence for problem P1.1

h	p			
	1	2	3	4
Order of convergence – surface elevation				
h_1	–	–	–	–
h_2	1.9261	3.1312	3.8957	5.1158
h_3	1.9869	3.0562	3.9527	5.0569
h_4	1.9432	3.0314	3.9779	4.8490
Order of convergence – velocity				
h_1	–	–	–	–
h_2	1.7802	3.1566	4.0082	4.4423
h_3	1.8605	2.9898	4.0104	5.0569
h_4	1.9265	3.0107	4.0038	5.4054

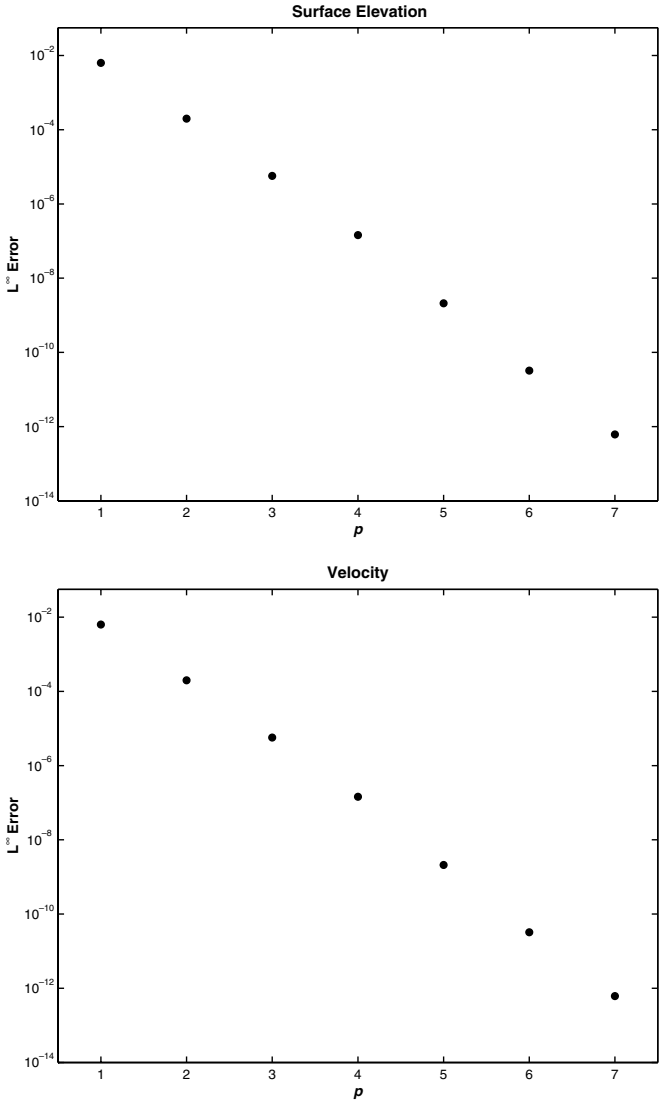

Fig. 5. p Convergence for problem P1.1 in surface elevation and velocity.

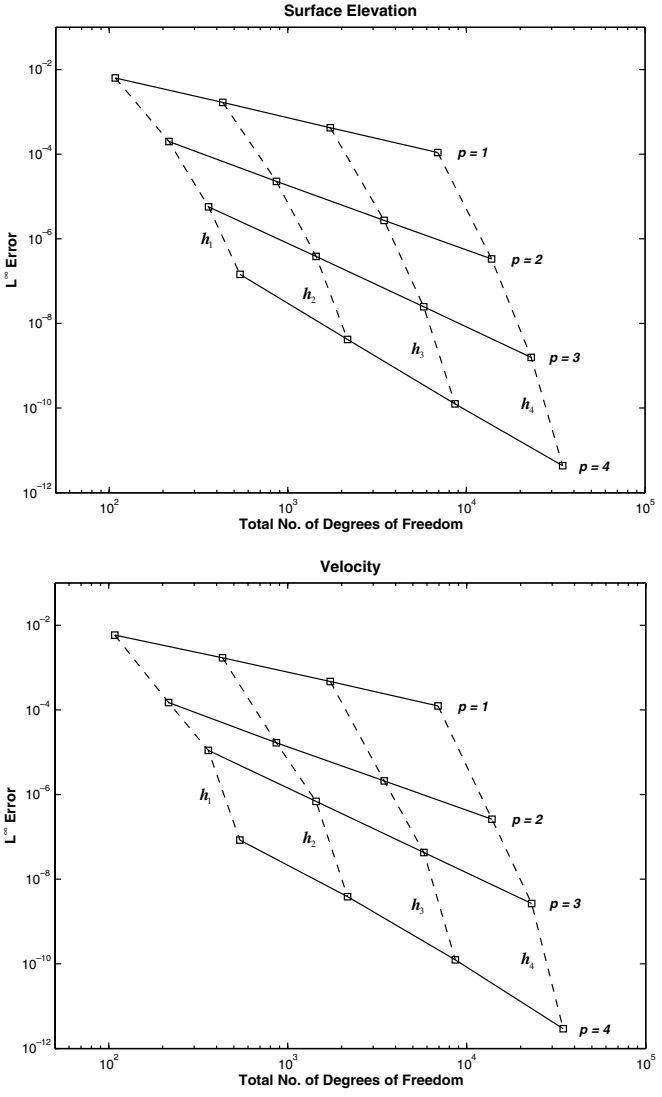

Fig. 6. hp Convergence for problem P1.1 in surface elevation and velocity.

The error is computed at $t = 2$ days by comparing the numerical solutions to the analytical solutions.

First, we examine the h convergence properties of the method by fixing p and varying h by systematically refining the grid as shown in Fig. 3. Errors are plotted as a function of h on a log–log scale for a range of p values in Fig. 4 for problem P1.1. The numerical rates of convergence are tabulated in Table 1 where it can be observed that optimal convergence rates of approximately $p + 1$ are observed in both the surface elevation and the velocity. We note that the slight degradation of the convergence rate in the surface elevation computed from h_3 to h_4 for $p = 4$ is due to the fact that the errors are on the order of machine precision.

Next, the p convergence properties of the method are investigated by fixing h and varying p. In Fig. 5, the error is plotted as a function of p on a linear-log scale for the first level of grid refinement where it can be noted that the expected exponential rate of convergence is obtained (observed as a straight line on the linear-log plot) in both the surface elevation and velocity solutions.

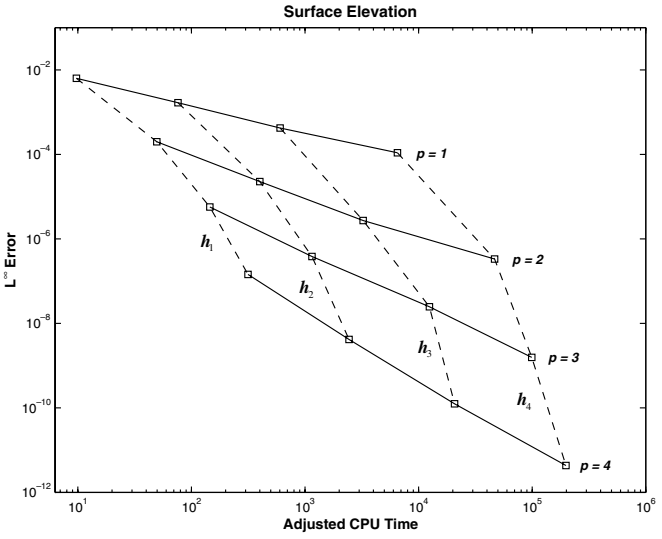

Fig. 7. Error in surface elevation vs. adjusted CPU times for problem P1.1.

The results of the h and p convergence studies can be combined on a single plot by plotting the error as a function of the total number of degrees of freedom. This is done in Fig. 6 where the solid lines indicate h refinement for a fixed p and the dashed lines indicate p refinement for a fixed h. For a given number of degrees of freedom the higher-order elements have lower error levels. Given

Table 2
Computed orders of convergence for problem P1.2

h	p			
	1	2	3	4
Order of convergence – surface elevation				
h_1	–	–	–	–
h_2	2.1279	3.0108	3.9582	5.0369
h_3	1.9920	3.0137	3.9799	4.9143
h_4	1.9728	3.0090	3.9899	4.7265
Order of convergence – velocity				
h_1	–	–	–	–
h_2	1.9784	3.1344	3.7027	5.0271
h_3	2.0080	2.8752	3.8994	5.1116
h_4	2.0038	2.9332	3.9505	4.3927

Table 3
Computed orders of convergence for problem P3

h	p		
	1	2	3
Order of convergence – surface elevation			
h_1	–	–	–
h_2	1.9318	3.2087	4.0215
h_3	1.9749	2.9825	3.9813
Order of convergence – velocity			
h_1	–	–	–
h_2	1.9236	3.2543	3.4405
h_3	1.9806	2.8696	3.9523

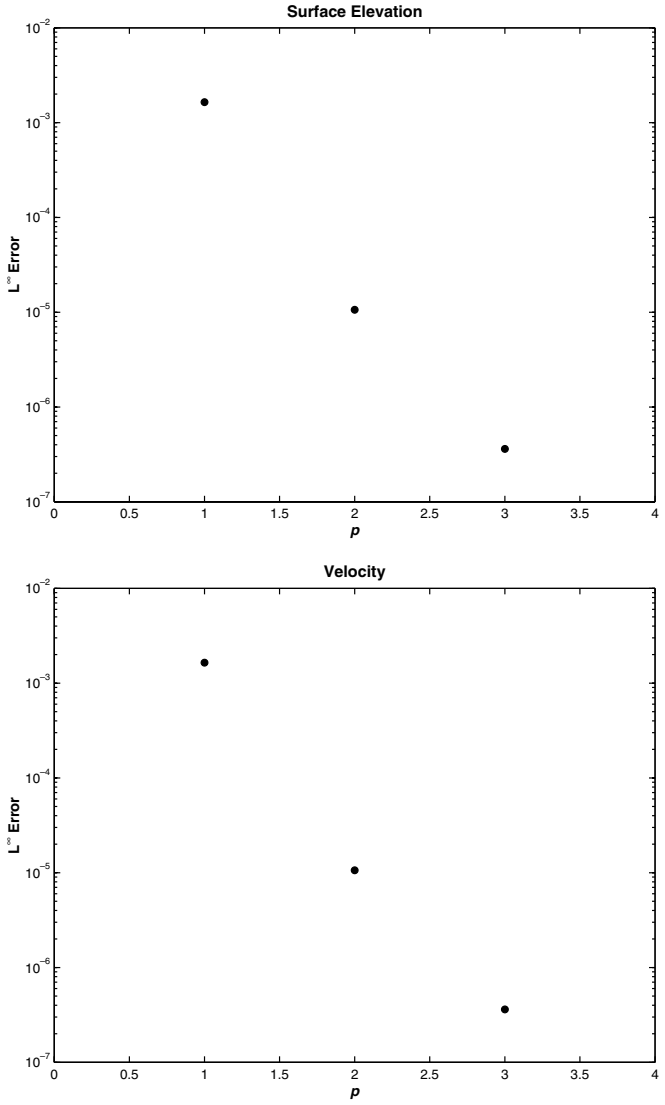

Fig. 9. p Convergence for problem P2 in surface elevation and velocity for grid refinement h_2.

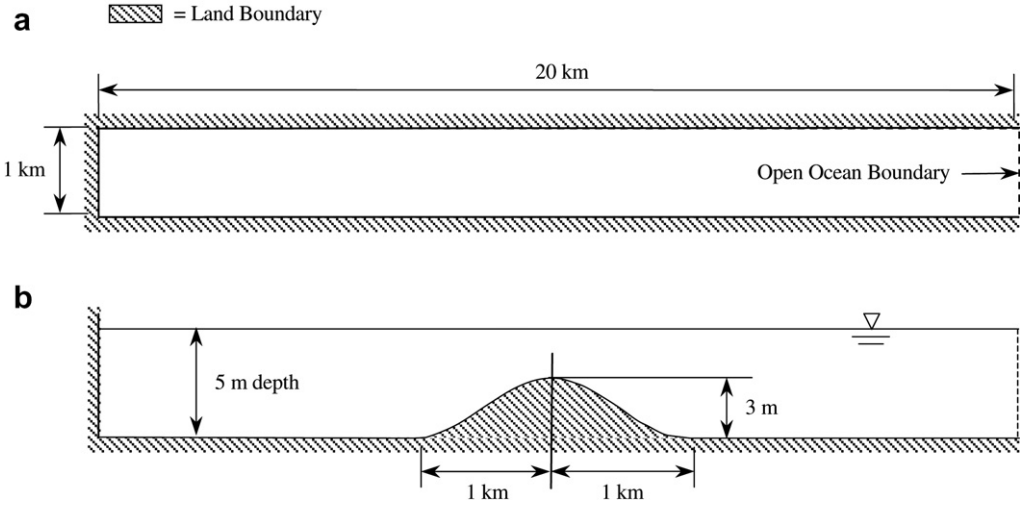

Fig. 8. Domain of problem P2: (a) plan view problem P2; (b) cross section of problem P2.

that the CPU time of a simulation is proportional to the total numbers of degrees of freedom, this suggests that using p refinement is significantly more efficient than using standard h refinement (at least, for smooth solutions as in this particular problem). This fact is verified in Fig. 7 where the error is plotted as a function of the estimated CPU time required for stability (see explanation below). Clearly, a given error level can be obtained in a shorter amount of time using p refinement rather than h refinement. As previously mentioned, the time steps used in these simulations were set arbitrarily small ($t = 1$ s) so that the spatial errors were certain to be the dominant contribution to the overall error. In order to compensate for this in analyzing the efficiency of the method, the CPU times used in plotting Fig. 7 have been adjusted based on the time step restriction given by Eq. (26) as follows: for $p = 1$ the CPU times for grid refinements h_2, h_3, and h_4 are multiplied by factors of 2, 4, and 8, respectively. For $p > 1$ the CPU times are adjusted by the factors for the grid refinement and by the ratio of the factor $(2p + 1)$ for the given p and $p = 1$, i.e. the factor $(2p + 1)/3$ which takes into account the additional reduction of the time step that is introduced by increasing p.

Finally, the results of problem P1.2, which includes linear bottom friction, are briefly summarized in Table 2. It can be noted that the convergence rates are very similar to problem P1.1 with rates of approximately $p + 1$ being obtained again. As with problem P1.1, we note again that the slight degradation of the convergence rates computed from h_3 to h_4 for $p = 4$ are due to machine precision.

4.2. Problem P2: Rectangular estuary with nonlinear SWE

In the previous set of test problems, the linear SWE were solved and the wave propagation characteristics of the solution were examined. With this problem, the full nonlinear SWE are solved as a means of rigorously assessing the performance of the method for flows with wave propagation and highly nonlinear advection dominance. In addition, there are nonlinear contributions from finite amplitude terms as well as bottom friction.

As with the previous problem, the domain is a rectangular harbor or channel surrounded on three sides by land boundaries with the remaining side on the east being an elevation specified open ocean boundary. The domain is 1 km wide in the north–south direction and 20 km long in the east–west direction. The bathymetry is flat at 5 m of depth with the exception of a 2 km long (in the east–west direction) 3 m amplitude sinusoidal bump in the center of the domain that runs the entire width of the channel (see Fig. 8). The problem is forced with a 1 m amplitude M_2 tidal signal. These conditions, both the bathymetry and large amplitude tidal forcing, are chosen to generate significant nonlinear components in the solution. Nonlinear bottom friction is also included where the bottom friction factor τ is given by

$$\tau = C_f \frac{\sqrt{u^2 + v^2}}{H}, \tag{33}$$

where C_f is the bottom drag coefficient (taken here to be $C_f = 0.003$). The problem is started from rest, and the

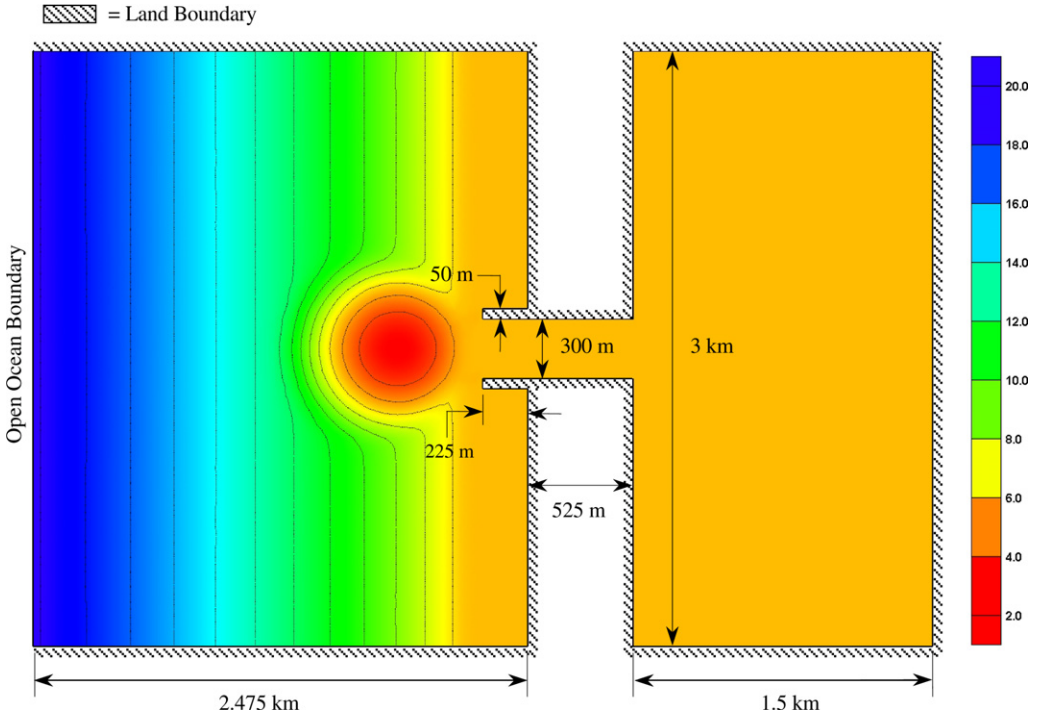

Fig. 10. Domain of problem P3.

amplitude of the tidal forcing at the open ocean boundary is slowly raised from 0 m to the full 1 m amplitude over the duration of half of a day using a hyperbolic tangent ramp function. The simulation time is 2 days.

Again, the h and p convergence properties of the method are investigated. Three levels of h and p refinement and are used: h= 200 m, 100 m, 50 m; and $p = 1, 2, 3$. For lack of an analytical solution, a coarse grid solution with $p = 7$ is used as the "exact" solution for the purposes of computing the error. The convergence results are presented in Table 3 where it can be observed that even for highly nonlinear flows h convergence rates of approximately $p + 1$ are still obtained for both the surface elevation and flow rates. Again, exponential convergence rates are obtained in the case of p-refinement as shown in Fig. 9.

4.3. Problem P3: Idealization of a coastal inlet with nonlinear SWE

In this problem, we examine the idealization of a typical coastal ocean modeling application, which gives rise to the formation and advection of strong eddies. The idealized

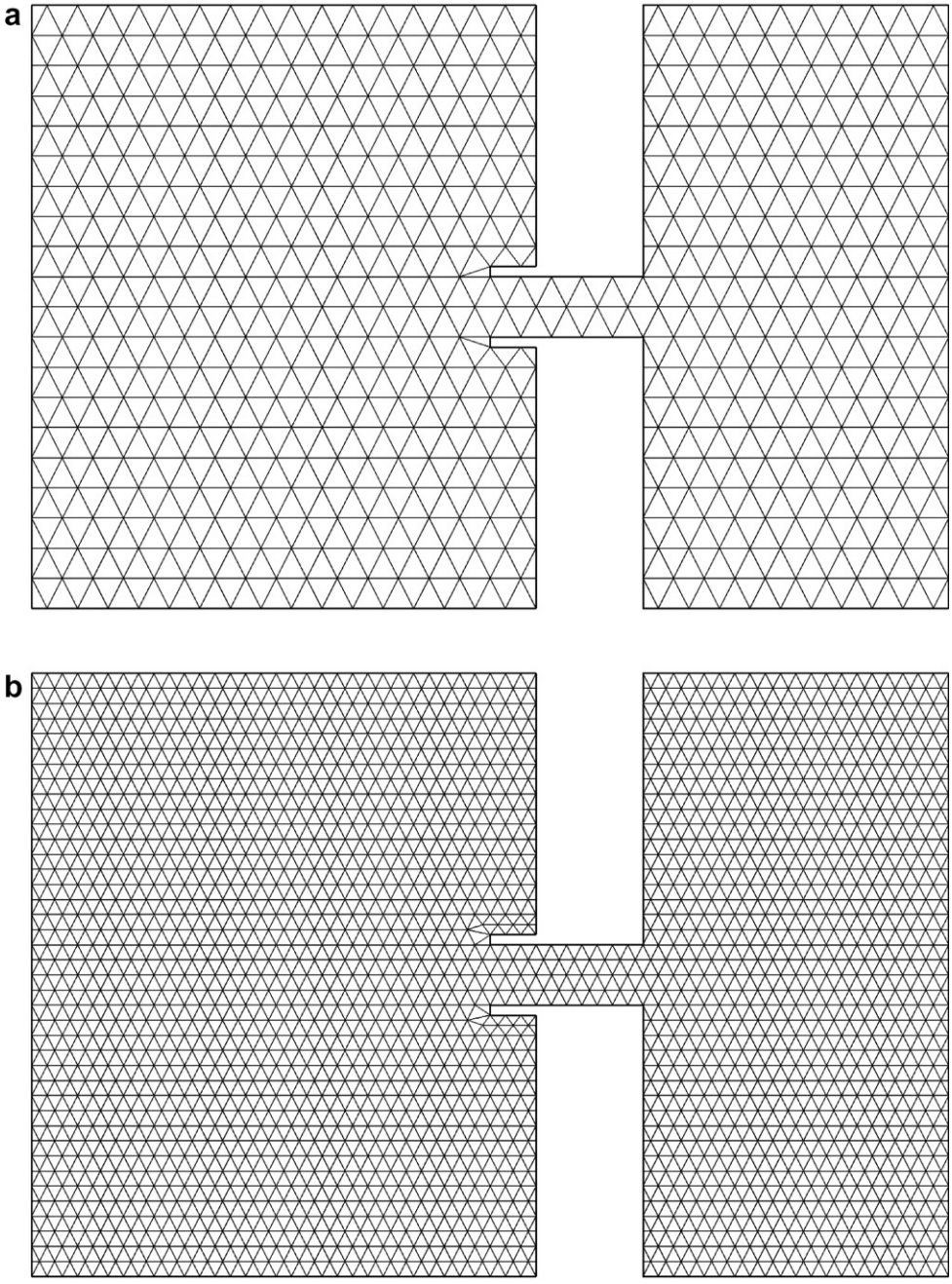

Fig. 11. Computational grids of problem P3: (a) grid h_1; (b) grid h_2.

domain is shown in Fig. 10, which consists of a back-bay that is connected to the open ocean to the west via an inlet with twin jetties. The bathymetry varies linearly from 19 m at the open ocean boundary to 5 m at the entrance of the inlet. Immediately to the west of the inlet is an ebb shoal approximately 750 m in diameter with a maximum height of 2 m at the center of the top. The formation of an ebb shoal is a common occurrence at coastal inlets and forms due to the deceleration of the flow as it exits the inlet system, which results in the deposition of large amounts of sediment that are being transported by the flow. In many instances, the growth of an ebb shoal can render a coastal inlet useless and returning it to operational status, through dredging operations, represents a significant cost to the agencies that maintain them. Sediment transport models (see for example [32]) can be used to analyze these systems, but rely on the input of an accurate representation of the flow field that resolves the fine-scale flow features of the problem such as the formation of eddies.

Traditionally, with h-versions of finite element SWE models, h-refinement would be added in the vicinity of the inlet, jetties, and the ebb shoal until a satisfactorily level of spatial resolution is achieved, which adequately captures the flow field. This is often a time consuming, iterative process and the level of h-refinement that is required can often result in a significant increase in the computational cost. However, as demonstrated in problem P1.1 the use of uniform p-refinement in DG methods offers an efficient alternative to adding h-refinement. Furthermore, the use of p-refinement simplifies the design of the computational grid, which would only be required to adequately resolve the geometry and the bathymetry of the problem.

Therefore, in this problem we investigate the use of uniform p-refinement versus uniform h-refinement in terms of resolving the fine-scale flow features of the problem. The problem is solved on two computational grids, a very coarse grid, h_1 that has only two elements across the width of the inlet and a finer grid, h_2 which is a refinement of grid h_1 (see Fig. 11). Using these computational grids the problem is solved using $p = 1, 2, 3,$ and 4. The simulations are run for a period of 3 days. A periodic M_2 tidal flow is specified uniformly along the open ocean boundary such that the maximum velocity in the throat of the inlet is approximately 1 m/s. The nonlinear bottom friction formulation as specified in the previous problem is used with $C_f = 0.003$.

The results of a typical simulation are shown in Fig. 12, which displays the velocity contours and vectors at four different stages of the tidal period. Fig. 12a and b show the formation and advection of eddies prior to and during the approximate time of maximum flood. Eddies form at the tips of the two jetties and are advected in an easterly direction being constrained by the walls of the inlet channel. This results in the elongated eddies seen in the western part of the channel. Large circular eddies can be observed in the back-bay at the exit of the inlet channel. These dual eddies form at the corners where the channel flows into the back-bay and are unconstrained and advect freely away from the channel into the back-bay. Fig. 12c and d show the flow prior to and during the approximate time of maximum ebb tide. During the ebb flow, eddies are formed at the corners of the channel and back-bay and advect in a westerly direction. Again these eddies are constrained by the channel walls and result in the elongated forms seen in the eastern part of the channel. The formation and advection of eddies off the jetty tips, away from the channel, and around the ebb shoal can also be observed. It is the combination of the inlet along with the presence of the jetties, channel and ebb shoal that creates a very complex, advection dominated flow scenario. It is critical to accurately compute these complex flow processes in order to correctly drive the transport of passive constituents and sediment around and through the inlet.

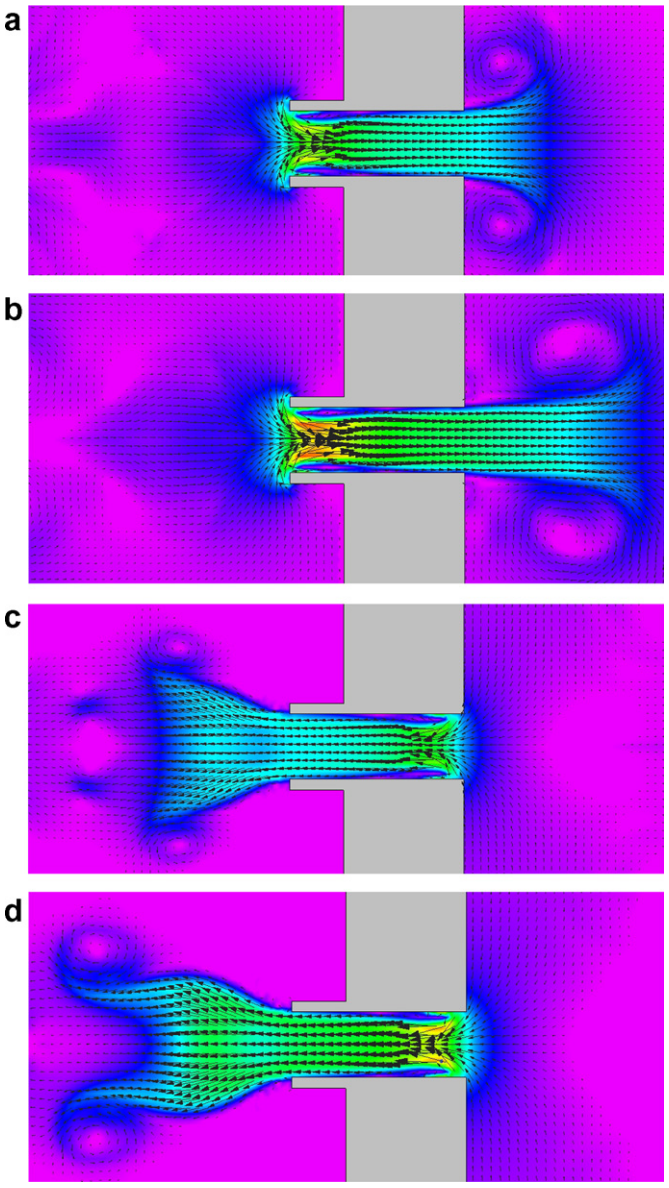

Fig. 12. Velocity contours and vectors for problem P3.

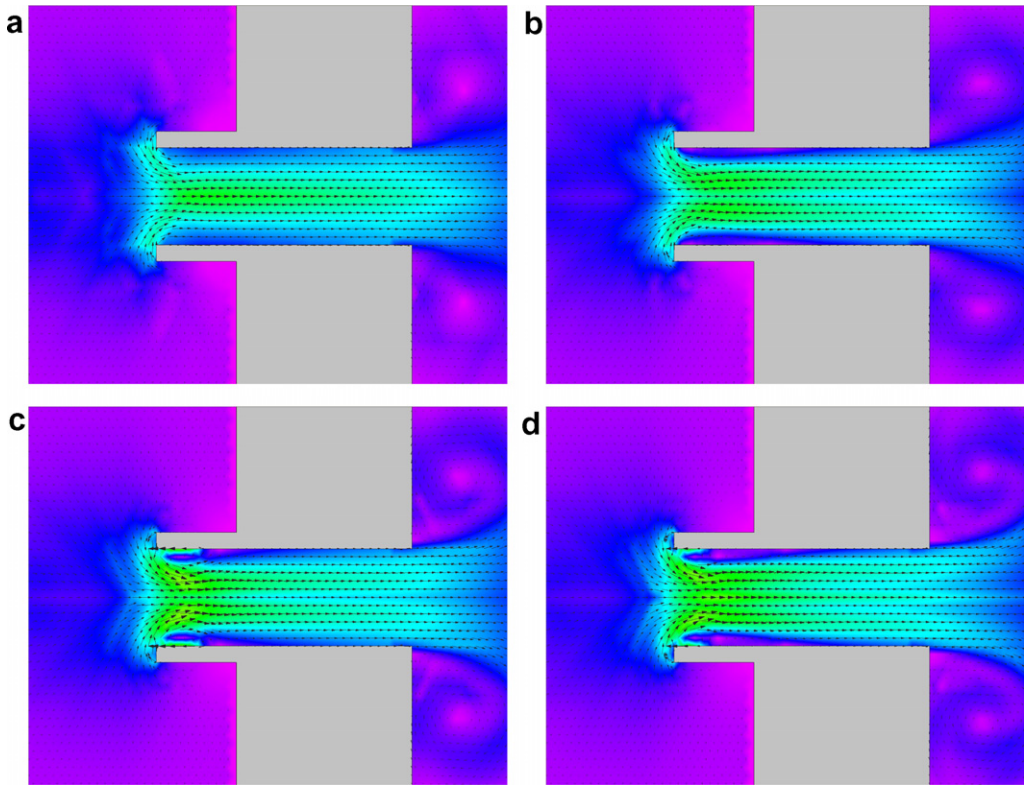

Fig. 13. Computed velocity contours and vectors for problem P3 using grid h_1 for (a) $p = 1$, (b) $p = 2$, (c) $p = 3$, and (d) $p = 4$.

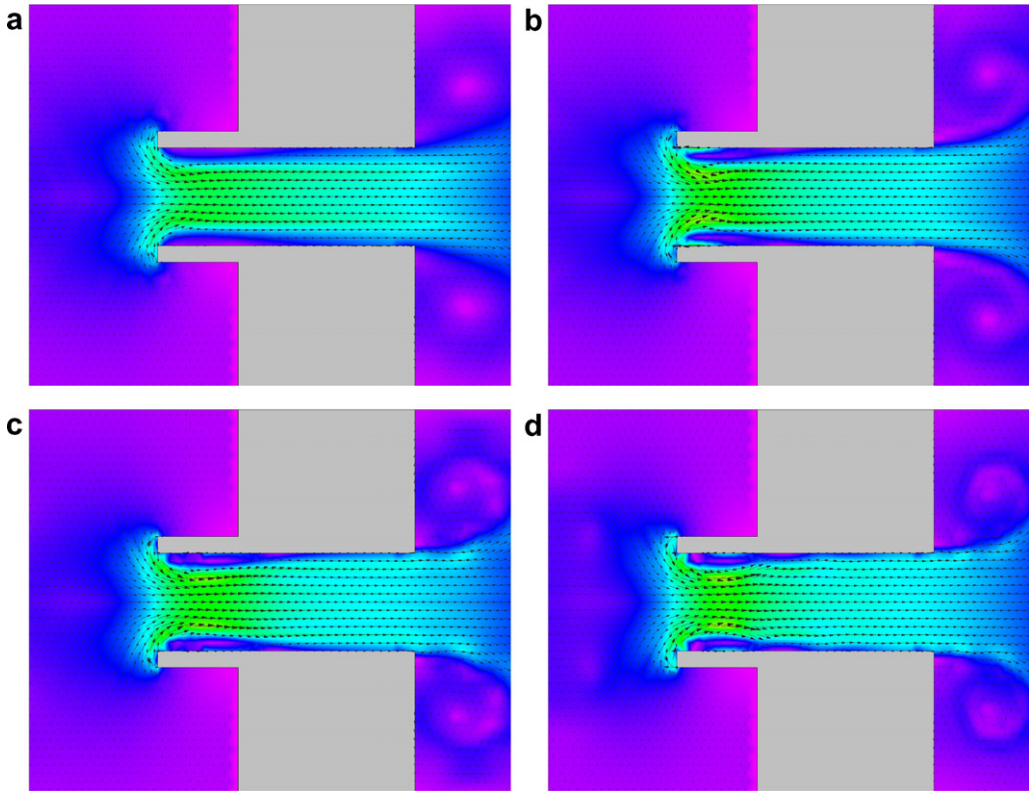

Fig. 14. Computed velocity contours and vectors for problem P3 using grid h_2 for (a) $p = 1$, (b) $p = 2$, (c) $p = 3$, and (d) $p = 4$.

In Fig. 13, the results with grid h_1 are shown using approximations of $p = 1$, 2, 3, and 4. It can be seen that the h_1, $p = 1$ solution does not supply the necessary spatial resolution along the interior of the channel to adequately capture the formation of the elongated eddies in the western part of the channel and the accompanying return flow. Additionally, the large circular eddies in the back-bay fail to be adequately resolved. Increasing to $p = 2$ provides some improvement, but the solution still fails to capture the complete formation of the eddies both in the back-bay and the channel, although some return flow can be seen along the sides of the channel. It can be seen that increasing to $p = 3$ provides significant improvement in resolving the structure of the eddies and strong return flow can be observed along the jetties in the western part of the channel. Finally, while the $p = 4$ solution provides some additional improvement, it is qualitatively similar to the $p = 3$ solution.

In Fig. 14, the results with grid h_2 are shown again using approximations of $p = 1$, 2, 3, and 4. The results for the h_2, $p = 1$ solution are qualitatively very similar to those for the h_1, $p = 2$ solution. However, it is interesting to note that this simulation took approximately twice as long (2.03×) to run as the h_1, $p = 2$ solution. Likewise, the results for the h_2, $p = 2$ solution are qualitatively very similar to the h_1, $p = 3$ solutions but took nearly 4 times longer (3.91×). Finally, the eddies are nicely resolved with the h_2, $p = 3$ and $p = 4$ solutions, however, it appears that the h_2, $p = 4$ solution may be exhibiting slight oscillations indicating perhaps that the $p = 3$ solution may be optimal for this problem at this level of grid resolution. As we found for problem P1.1, the use of uniform p-refinement offers a more efficient means of obtaining more accurate solutions than using uniform h-refinement even for flows exhibiting complex, two-dimensional flow structures.

Finally, we compare the results obtained using the DG method for this problem with results obtained from a widely used CG based SWE model, ADCIRC [5]. Briefly, ADCIRC solves a reformulation of the SWE (the continuity equation is replaced by the so-called generalized wave continuity equation (GWCE), see for example [4]) using a CG finite element method in space and implicit/explicit time stepping (see [5] for details). ADCIRC has been validated in a large number of test cases (see for example [33–36]), though, historically it has shown deficiencies in advection dominated flow scenarios unless eddy viscosity is added to the equations and/or much finer computational grids than the ones presented here are used. Fig. 15a and b show the velocity contours and vectors produced by ADCIRC (using grid h_2 and $p = 1$) during the approximate time of maximum flood and ebb tide, respectively. It can be seen that severe oscillations are present in the velocity field in the back-bay and in the open ocean in the vicinity of the jetties and the ebb shoal. Furthermore, the solution fails to adequately resolve the structure of the eddies (compare to Fig. 13).

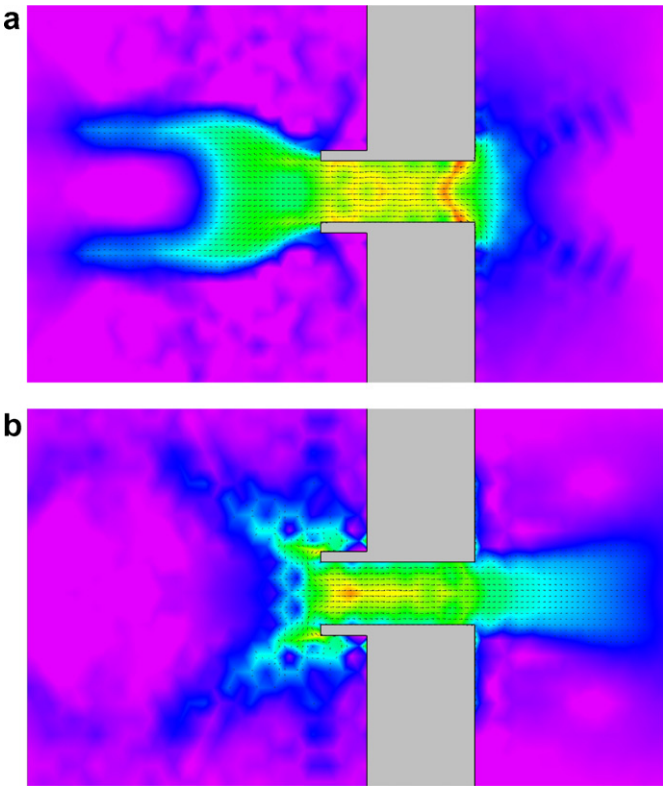

Fig. 15. ADCIRC velocity contours and vectors for problem P3 using grid h_2.

5. Conclusions and discussion

In this paper, we have presented our implementation of an *hp* DG method for the solution of the two-dimensional SWE. Specific details were included on the implementation of the method, and we examined the performance of the method for both linear wave propagation problems and highly nonlinear wave propagation problems with advection dominance. It was shown that the DG solutions excelled at solving these problems with both low- and high-orders of p, and the h and p convergence properties of the method were demonstrated for both linear and highly nonlinear problems.

We have also shown the ability of the method to resolve the advection of eddies in a tidal inlet with jetties and an ebb shoal. These solutions were computed with very coarse levels of resolution without specifying any eddy viscosity or applying slope limiters. We note that the CG based solutions to this problem, as demonstrated, had significant robustness and accuracy problems with the coarse levels of resolution used in our computations.

The problems studied also indicate that highly nonlinear problems perform very well with high levels of p. This includes the highly advection dominated tidal inlet problem. The DG method ably captured the relevant constrained and unconstrained eddies that are generated and advected in this problem. It is clear that high-order DG solutions have the flexibility to locally form and advect the critical flow struc-

tures without over-constraining adjacent elements leading to a cascading of oscillations resulting from high-order interpolation as can be the case in CG methods.

Finally, it appears that there are significant cost efficiency benefits in using high-order p solutions for both smooth and rapidly spatially varying flows. The exponential convergence rates that are obtained using p-refinement with the DG method indicate the efficiency advantages in applying p-refinement instead of h-refinement even in highly nonlinear, two-dimensional flow scenarios. Future work in this area involves implementing a p-adaptive strategy to locally refine solutions dynamically in time.

Acknowledgements

This work was supported by the Morphos – 3D Long Wave Hydrodynamics Modeling Work Unit funded through Woolpert Inc. by the US Army Corps of Engineers, Mobile District under contract W91278-05-D-0018/003.

References

[1] G.W. Platzman, Some response characteristics of finite element tidal models, J. Comput. Phys. 40 (1981) 36–63.
[2] W.G. Gray, D.R. Lynch, On the control of noise in finite element tidal computations, Comput. Fluids 7 (1979) 47–67.
[3] J.H. Atkinson, J.J. Westerink, R.A. Luettich, Two-dimensional dispersion analyses of finite element approximations to the shallow water equations, Int. J. Numer. Methods Fluids 45 (2004) 715–749.
[4] D.R. Lynch, W.G. Gray, A wave equation model for finite element tidal computations, Comput. Fluids 7 (1979) 207–228.
[5] R.A. Luettich, J.J. Westerink, Formulation and Numerical Implementation of the 2D/3D ADCIRC finite element model version 44.XX, 2004. Available from: <www.marine.unc.edu/C_CATS/adcirc/adcirc_theory_2004_05_14.pdf>.
[6] J.M. Hervouet, On spurious oscillations in primitive shallow water equations, in: L.R. Bentley et al. (Eds.), Proceedings of the XIII International Conference on Computational Methods in Water Resources, vol. II, Balkema Publishers, Rotterdam, 2000, pp. 929–936.
[7] S.W. Bova, G.F. Carey, A symmetric formulation and SUPG scheme for the shallow-water equations, Adv. Water Resour. 19 (1996) 123–131.
[8] J.C. Galland, N. Goutal, J.M. Hervouet, TELEMAC: a new numerical model for solving shallow water equations, Adv. Water Resour. 14 (1991) 138–148.
[9] W.H. Reed, T.R. Hill, Triangular meshes methods for the neutron transport equation, Technical PaperLA-UR-73-479, Los Alamos Scientific Laboratory, 1973.
[10] D. Schwanenberg, R. Kiem, J. Kongeter, Discontinuous Galerkin method for the shallow water equations, in: B. Cockburn, G.E. Karniadakis, C.W. Shu (Eds.), Discontinuous Galerkin Methods, Springer, Heidelberg, 2000, pp. 289–309.
[11] H. Li, R. Liu, The discontinuous Galerkin finite element method for the 2D shallow water equations, Math. Comput. Simul. 56 (2001) 223–233.
[12] V. Aizinger, C. Dawson, A discontinuous Galerkin method for two-dimensional flow and transport in shallow water, Adv. Water Resour. 25 (2002) 67–84.
[13] D. Schwanenberg, M. Harms, Discontinuous Galerkin finite-element method for transcritical two-dimensional shallow water flows, J. Hydraul. Engrg. 130 (2004) 412–421.
[14] S. Fagherazzi, P. Rasetarinera, M.Y. Hussaini, D.J. Furbish, Numerical solution of the dam-break problem with a discontinuous Galerkin method, J. Hydraul. Engrg. 130 (2004) 532–539.
[15] F.X. Giraldo, J.S. Hesthaven, T. Warburton, Nodal high-order discontinuous Galerkin methods for the spherical shallow water equations, J. Comput. Phys. 181 (2002) 499–525.
[16] C. Eskilsson, S.J. Sherwin, A triangular spectral/*hp* discontinuous Galerkin method for modelling 2D shallow water equations, Int. J. Numer. Methods Fluids 45 (2004) 605–623.
[17] R.D. Nair, S.J. Thomas, R.D. Loft, A discontinuous Galerkin global shallow water model, Mon. Weather Rev. 133 (2005) 876–888.
[18] T.C. Warburton, G.E. Karniadakis, A discontinuous Galerkin method for the viscous MHD equations, J. Comput. Phys. 152 (1999) 608–641.
[19] C. Dawson, J. Proft, Discontinuous and coupled continuous/discontinuous Galerkin methods for the shallow water equations, Comput. Methods Appl. Mech. Engrg. 191 (2002) 4721–4746.
[20] R.J. LeVeque, Numerical Methods for Conservation Laws, Birkhauser Verlag, Basel, 1992.
[21] P.L. Roe, Approximate Riemann solvers, parameter vectors, and difference schemes, J. Comput. Phys. 43 (1981) 357–372.
[22] B. Cockburn, S.Y. Lin, C.W. Shu, TVB Runge–Kutta local projection discontinuous Galerkin finite element method for conservation laws III: one-dimensional systems, J. Comput. Phys. 84 (1989) 90–113.
[23] M. Dubiner, Spectral methods on triangles and other domains, J. Scientific Comput. 6 (1998) 345–390.
[24] H.L. Atkins, C.W. Shu, Quadrature-free implementation of discontinuous Galerkin methods for hyperbolic equations, AIAA J. 36 (1998) 775–782.
[25] B. Cockburn, C.W. Shu, The Runge–Kutta discontinuous Galerkin finite element method for conservation laws V: Multidimensional systems, J. Comput. Phys. 141 (1998) 199–224.
[26] I. Lomtev, B. Quillen, G.E. Karniadakis, Spectral/*hp* methods for viscous compressible flows on unstructured 2D meshes, J. Comput. Phys. 144 (1998) 325–357.
[27] D.A. Dunavant, High degree efficient symmetrical Gaussian quadrature rules for the triangle, Int. J. Numer. Methods Engrg. 21 (1985) 1129–1148.
[28] C.W. Shu, S. Osher, Efficient implementation of essentially non-oscillatory shock-capturing schemes, J. Comput. Phys. 77 (1988) 439–471.
[29] C.W. Shu, TVB uniformly high-order schemes for conservation laws, Math. Comput. 49 (1987) 105–121.
[30] B. Cockburn, C.W. Shu, Runge–Kutta discontinuous Galerkin methods for convection-dominated problems, J. Scientific Comput. 16 (2001) 173–261.
[31] D.R. Lynch, W.G. Gray, Analytical solutions for computer flow model testing, J. Hydraul. Div. HY10 (1978) 1409–1428.
[32] E.J. Kubatko, J.J. Westerink, C. Dawson, An unstructured grid morphodynamic model with a discontinuous Galerkin method for bed evolution, Ocean Modell., in press.
[33] C.A. Blain, J.J. Westerink, R.A. Luettich, The influence of domain size on the response characteristics of a hurricane storm surge model, J. Geophys. Res. 99 (1994) 18467–18479.
[34] C.A. Blain, J.J. Westerink, R.A. Luettich, Grid convergence studies for the prediction of hurricane storm surge, Int. J. Numer. Methods Fluids 26 (1998) 69–401.
[35] A. Mukai, J.J. Westerink, R.A. Luettich, D.J. Mark, A tidal constituent database for the western north Atlantic Ocean, Gulf of Mexico and Caribbean Sea, Technical Report, US Army Engineer Research and Development Center, Vicksburg MS, Report ERDC/CHL TR-02-24.
[36] J.J. Westerink, R.A. Luettich, J.C. Muccino, Modeling tides in the western north Atlantic using unstructured graded grids, Tellus 46A (1994) 178–199.